Chemical, Structural and Electronic Characterization of the (010) Surface of Single Crystalline Bismuth Vanadate

Marco Favaro,[†] Reinhard Uecker,[‡] Silvia Nappini,[§] Igor Píš,[§,∥] Elena Magnano,[§,⊥] Hendrik Bluhm,[#,¶] Roel van de Krol,[†] and David E. Starr*[,†]

[†] *Institute for Solar Fuels, Helmholtz-Zentrum Berlin für Materialien und Energie GmbH, 14109, Berlin, Germany.*

[‡]*Leibniz Institut für Kristallzüchtung (IKZ), Max-Born-Str. 2, 12489, Berlin, Germany*

[§] *IOM CNR, LABORATORIO TASC, S.S, 14 km 163.5, I-34149 Basovizza (TS), Italy.*

[∥] *Elettra-Sincrotrone Trieste S.C.p.A., S.S, 14 km 163.5, I-34149 Basovizza (TS), Italy.*

[⊥] *Department of Physics, University of Johannesburg, PO Box 524, Auckland Park 2006, South Africa.*

[#] *Advanced Light Source, Lawrence Berkeley National Laboratory, Berkeley, CA 94720, USA.*

[¶] *Chemical Sciences Division, Lawrence Berkeley National Laboratory, Berkeley, CA 94720, USA.*

ABSTRACT:

We have structurally, chemically and electronically characterized the most stable (010) surface of a Mo-doped $BiVO_4$ single crystal. Low energy electron diffraction (LEED) reveals that the surface is not significantly reconstructed from a bulk termination of the crystal. Synchrotron based X-ray spectroscopies indicate no surface enhancement of any of the crystal constituents and that the Mo dopant occupies tetrahedral sites by substituting for V at the surface. Using resonant photoemission to study the valence band structure as the V L_3 edge is scanned we observe an intra-band gap state associated with reduced vanadium formed by the Mo doping. This state is likely associated with small polaron formation at the surface. This feature is enhanced at a photon energy that is not resonant with any of the main features in the absorption spectrum of the pristine $BiVO_4$. This indicates that the additional electron from Mo doping likely induces further distortion of the VO_4 tetrahedral units and generates a new conduction band state either by splitting of the V dz^2 states or by hybridization of V d_{zx} and V dz^2 states. We measure a work function of 5.15 eV for the $BiVO_4$(010) surface. Measurement of the work function allows us to recast the electronic energy levels onto the normal hydrogen electrode scale for comparison to the standard reduction and oxidation potentials of water. This detailed study should provide a basis for future work aimed at a molecular level understanding of $BiVO_4$/electrolyte interfaces used for photoelectrochemical water splitting.

Introduction

One of the greatest obstacles to the widespread adoption of solar energy is its intermittency. Producing chemical fuels using sunlight (i.e., solar fuels) is a potential way to store solar energy and mitigate this intermittency.[1, 2, 3, 4] Despite increasing interest in the direct conversion of solar light into liquid fuels by photoelectrochemically reducing carbon dioxide,[5, 6, 7] solar fuel research to date has primarily focused on photoelectrochemical water splitting to produce hydrogen (H_2O + sunlight $\rightarrow$ H_2 + O_2). The generated hydrogen can be used as a primary energy source (e.g., in hydrogen fuel cells) or for the production of synthetic fuels via Fischer-Tropsch synthesis.[8, 9, 10, 11, 12, 13, 14] The successful implementation of solar hydrogen into the energy landscape would further spread the usage of solar energy technologies and could potentially secure a large fraction of the world's future energy needs.

Water oxidation is currently viewed as the major limitation to efficient solar water splitting. As a result, material research efforts focus mainly on photoanodes for the oxygen evolution reaction (OER). The material requirements for solar water splitting photoanodes are quite demanding. First, the valence band maximum (VBM) of the semiconductor must be lower than the oxygen evolution potential (+1.23 V vs. normal hydrogen electrode, NHE, at pH 0) to allow holes to transfer to the electrolyte and oxidize water. Secondly, the semiconducting material should have a band-gap between 1.5 and 2.5 eV to harvest a significant fraction of the solar spectrum, and develop enough photovoltage to sustain water splitting (1.5-1.8 V).[4] Finally, the material must be stable for years under illumination in aqueous electrolyte solution, over a broad temperature range. Due to their strong potential for satisfying these criteria, multinary semiconducting metal oxides are currently being investigated as water splitting photoanode materials.[15]

Bismuth vanadate ($BiVO_4$), a ternary metal oxide, is currently viewed as among the most promising of multinary semiconducting metal oxides for solar water splitting.[9, 10, 16, 17, 18, 19] $BiVO_4$ is an *n*-type semiconductor with an indirect band-gap of 2.4 – 2.5 eV,[20, 21, 22] implying that approximately 11 % of the solar spectrum can be harvested. Recent reports of about 8% solar to hydrogen (STH) conversion efficiency in a hybrid photovoltaic/photoelectrochemical device under AM 1.5 illumination places it among the most successful oxide photoanodes to date.[23, 24] $BiVO_4$, however, suffers from high charge carrier recombination rates and limited charge mobility due to polaron formation. Since water splitting is ultimately an interfacial chemical process, the performance of $BiVO_4$ photoanodes may be further limited by the analogous surface

processes; charge recombination at surface states and surface polaron formation through charge coupling to surface phonons.[25, 26, 27, 28, 29] Metal doping, in particular W and Mo doping, has been widely used to increase charge carrier conductivity and to reduce the band-gap of $BiVO_4$.[4, 15, 26] Theoretical studies have investigated the effects of doping on the bulk[30] and surface electronic properties of the monoclinic scheelite phase of $BiVO_4$.[31, 32, 33] These studies have shown that the (010) surface is the lowest energy surface and the natural cleavage plane.[32, 33] When doping with Mo, Ding et al. suggested that the Mo dopants selectively occupy Bi sites at the (010) surface, whereas it occupies V sites in the bulk of the material.[33] Further, the Mo dopant was calculated to be more stable at the surface than in the bulk which may lead to enhanced Mo concentrations at the surface. Luo et al. found that Mo doping led to Mo located at V sites throughout the material.[34] Interestingly, W and Mo doping of $BiVO_4$ leads to the formation of intra-band gap states. These states have been attributed to the localization of the excess electron in V 3d valence orbitals (most likely of *e* symmetry) which formally changes the oxidation state of V from V^{5+} to V^{4+} and leads to the formation of localized small polaron states.[22, 32, 35] Small polaron states may be responsible for the higher charge recombination rates observed for doped $BiVO_4$ compared to undoped $BiVO_4$. Recently, Jovic et al. verified the existence of intra-band gap states induced by Mo and W doping using resonant photoemission spectroscopy (ResPES) and inelastic X-ray scattering (RIXS) on single crystalline metal doped $BiVO_4$ in ultra-high vacuum (UHV) conditions.[22, 35]

In this paper, we structurally, chemically and electronically characterize the most stable (010) surface of $BiVO_4$ single crystals. The power of single crystal surface studies stems from their atomically well-defined nature. Due to the rarity of $BiVO_4$ single crystals, experiments on well-defined $BiVO_4$ surfaces are limited and the current study should provide a basis for future work aimed at a molecular-level understanding of $BiVO_4$/aqueous electrolyte interfaces used for solar water splitting. Our crystals are doped with ~1% Mo to increase their conductivity and facilitate surface sensitive experiments that use charged particles (electrons and/or ions). We demonstrate that a clean, carbon free and well-structured surface can be prepared via a simple vacuum annealing and re-oxidation procedure. Low energy electron diffraction (LEED) measurements show that the clean (010) facet exhibits an unreconstructed 1×1 surface. Quantitative X-ray photoelectron spectroscopy (XPS) analysis reveals the expected surface chemical composition for the nominally 1 at.% Mo doped $BiVO_4$. Using a combination of surface sensitive X-ray photoelectron spectroscopy (XPS) and X-ray absorption spectroscopy (XAS), we show that V is

predominantly present as V^{5+} in a distorted tetrahedral coordination site, and that the Mo dopant is present as Mo^{6+} in a tetrahedral geometry. This implies that Mo substitutes for V in the $BiVO_4$ surface. ResPES performed at the V L_3 edge in UHV conditions shows the existence of a localized state 0.91 eV above the valence band maximum (VBM). This state is attributed to the reduction of V^{5+} to V^{4+} by the Mo^{6+} ionized dopants and the formation of small polaron states which cause re-hybridization of conduction band states. Lastly, work function measurements allow us to put our measured energy levels on the NHE scale for direct comparison to the standard water oxidation and reduction potentials.

Experimental

Crystal Growth

The starting oxides Bi_2O_3, V_2O_5 and MoO_3 were of a minimum 99.99% purity. To prepare the starting melt, the powders were dried, mixed in the stoichiometric ratio, sintered and finally isostatically pressed following standard procedures. The crystals were grown by the conventional Czochralski technique with RF-induction heating and automatic diameter control. Because of the low melting temperature of $BiVO_4$ (1213 K), platinum crucibles were used as the melt container. This means that the crystals could be grown in air. To adjust the required temperature gradients, an active afterheater was installed above the crucible. The crucible dimensions were 40mm in diameter and height; the afterheater was of the same diameter and 70 mm in height. Thermal insulation was provided by an outer alumina ceramic tube filled with alumina granules. The seed crystal was obtained from spontaneously crystallized material. The pulling rate was 1.0 mm h^{-1} and the rotation rate was 10 rpm. After growth, the crystal was cooled down to room temperature over 20 h. The resulting crystal was of 77 mm in length and 18 mm in diameter.

Surface Preparation

Approximately 5 mm x 5 mm x 5 mm Mo-doped (nominally 1 at.%) $BiVO_4$ samples were cut from the bulk crystal. The sample was first cleaved on the bench top parallel to the (010) plane. The sample was then thoroughly rinsed with high purity ethanol (Aldrich, > 99.99%) and Milli Q water (ρ=18.2 M$\Omega \cdot$ cm), blown dry with N_2(g) and introduced into the vacuum chamber. Once introduced into the chamber, the sample was heated to 300° C for 60 min in UHV (~ 10^{-9} Torr) and then cooled down to room temperature. The sample was then heated to 300° C in 1.0 Torr of O_2(g) and then cooled down again to room temperature. The optimal heating duration in O_2(g) was determined by *in situ* monitoring and minimization of the C 1s signal. X-ray photoelectron spectroscopy (XPS) revealed that this procedure produces a clean, well-ordered surface with no indication of Mo surface segregation. The absence of surface carbon contamination was verified by the lack of a signal in the C 1s core level spectrum upon returning to room temperature and UHV conditions (**Figure S1**). Low energy electron diffraction (LEED) patterns were acquired after each preparation cycle, to control the surface orientation and structure.

Soft X-ray photoelectron, resonant photoelectron and absorption spectroscopies

The experiments were conducted at two end-stations located at two different synchrotrons.

Beamline 11.0.2 at the Advanced Light Source

The end-station of beamline 11.0.2 at the Advanced Light Source (Lawrence Berkeley National Laboratory, Berkeley, U.S.A.) was used for XPS, resonant photoemission spectroscopy (ResPES) and partial electron yield near edge X-ray absorption (PEY−NEXAFS) measurements. The source for the beamline is an elliptically-polarized undulator delivering photons from 90 eV up to ~1600 eV.[36] The pressure in the experimental chamber was kept under ultra-high vacuum conditions (UHV, pressure ~10^{-9} Torr). The experimental endstation is equipped with a Near Ambient Pressure Phoibos 150 electron analyzer (SPECS).

XPS, ResPES and PEY-NEXAFS measurements were carried out in the dark and at room temperature with the electron energy analyzer placed at the magic angle (54.7°) between the X-ray polarization vector and the photoelectron momentum vector. The photoelectrons had a take-off angle of 47° from the surface normal.[36] The X-ray polarization was horizontal for all measurements.

The XPS data (valence band (VB) and Au 4f, Bi 4f, Mo 3d, C 1s, V 2p and O 1s core levels) were acquired using a photoelectron kinetic energy (KE) of 200 eV, a step size of 0.05 eV and a pass energy of 20 eV. We used 10 x 50 μm^2 (dispersive x non-dispersive) slit widths for all measurements. Under these conditions, the total resolution (beamline and electron analyzer) was better than 100 meV at 735 eV at room temperature as measured by the Au $4f_{7/2}$ full-width at half-maximum (FWHM). At KE=200 eV the photoelectron inelastic mean free path (λ_e) in $BiVO_4$, determined with the "simulation of electron spectra for surface analysis" software (SESSA),[37] was equal to ~8 Å. The nominal photon energies used to yield photoelectron KEs of about 200 eV were 365 eV for Bi 4f, 440 eV for Mo 3d, 490 eV for C 1s, 715 eV for V 2p, and 735 eV for O 1s. The corresponding photoionization cross sections (within the dipole approximation[38]) were 4.6 Mbarn for Bi 4f, 3.0 Mbarn for Mo 3d, 0.28 Mbarn for C 1s, 0.92 Mbarn for V 2p, and 0.25 Mbarn for O 1s.

The PEY-NEXAFS data (V $L_{2,3}$ and O K edges) were acquired using a photoelectron KE of 425 eV ($\lambda_e \sim$ 13 Å). The analyzer pass energy was set to 100 eV, giving an energy window of ±10 eV around the KE setpoint. The photon energy step was set to 0.1 eV, and the integration time was 1.0 s. The beamline resolution was better than 0.1 eV.

The ResPES measurements across the V $L_{2,3}$ were conducted by acquiring VB spectra as the V L_3 edge was scanned. The photon energy was scanned in steps of 0.1 eV. The VB spectra were acquired with a photoelectron KE step of 0.05 eV and an integration time of 0.3 s.

BACH beamline at the Elettra synchrotron

The BACH beamline (Beamline for Advanced diCHroism) is served by two APPLE-II elliptical undulators that are used alternatively in order to optimize the flux with respect to the selected photon energy. The beamline delivers photons with energy in the range of 35-1650 eV.[39] The end-station is equipped with a Scienta R3000 spectrometer. All experiments were conducted in UHV at pressures < 5 x 10^{-10} mbar.

NEXAFS measurements performed at the BACH beamline used the total electron yield (TEY) detection mode. TEY-NEXAFS was performed in UHV (pressure ~10^{-10} Torr), in the dark and at room temperature with horizontally linearly polarized light under grazing incidence ('out of plane') conditions. The take-off angle was set to 20° from the surface normal. The PE step was set to 0.1 eV, and the integration time set to 1.0 s. At room temperature the spectral resolution was less than 0.1 eV.

The work function (φ) measurements were carried out at a nominal photon energy of 47 eV (horizontal polarization) and normal emission. The angle between the Poynting vector of the radiation and the electron analyzer was equal to 60°. The pass energy was set to 5 eV and the overall spectral resolution (beamline and electron analyzer) was better than 0.02 eV at room temperature.

Spectra Calibration

The binding energy (BE) scale for the core level and VB spectra was calibrated using the Au 4f photoelectron peak from a clean gold polycrystalline surface as a reference ($4f_{7/2}$ BE = 84.0 eV). This is valid as long as there is no band bending or charging of the sample. **Figure S2** shows normalized and calibrated Bi 4f core level spectra acquired at different photon energies: 360 eV, 520 eV and 735 eV. Each spectrum has a different information depth, photoionization cross section and photon flux. Since no binding energy shifts or differences in peak broadening are observed we can exclude the presence of band bending on the clean surface. Sample charging is typically a function of the photon flux and the photon energy dependent photoionization cross-section. The flux at a photon energy of 520 eV was about 1.3-times higher than that at 360 eV, whereas the flux at a photon energy of 735 eV was about 10% of that at 360 eV. The absence of any detectable change in the Bi 4f core level spectra with changes in the photon energy indicates that the sample does not significantly charge during photoemission measurements. Lastly, LEED patterns were readily obtained from the sample further indicating that the sample does not appreciably charge.

For the ResPES data the initial photon energy (PE) was calibrated by acquiring the Bi 4f spectrum of the Mo(1 at.%):$BiVO_4$ sample with the first and the second order light of the chosen photon energy; the photon energy was assumed to be equal to the difference in kinetic energy of the Bi $4f_{7/2}$ peak for the spectra acquired with first and second order light. The final photon energy was calibrated by acquiring a Bi 4f spectrum at the final photon energy (1^{st} order only) and assuming the kinetic energy difference between the initial and final Bi 4f spectra taken with 1^{st} order light was equal to the difference in photon energy. Binding energies of the VB spectra were calibrated by periodically taking Bi 4f spectra at specific photon energies and using its calibrated BE as a reference value.

The photon energies for the NEXAFS measurements were calibrated using the known XAS resonance positions of O_2 gas.

Data Analysis

Quantitative PES was performed using the normalized integrated peak areas of each core level. The normalized areas were obtained by dividing the raw integrated core level peak area by the corresponding photoionization cross section (reported above for each core level) and photon flux. The photon flux was measured using a Si photodiode (Opto Diode, AXUV100G, 10 mm ×10 mm × 55 μm).

All fits reported in this work have been carried out using symmetrical pseudo-Voigt functions (G/L ratio ranging from 85/15 to 75/25) after Shirley background subtraction. During the fitting procedure, the Shirley background was optimized together with the spectral components, increasing the precision and reliability of the fitting procedure. [40, 41, 42] The VB was de-convoluted by subtracting the background and fitting with symmetrical Voigt functions (G/L ratio ranging from 85/15 to 95/5). The Tougaard background was chosen for the VB analysis.[43]

Results and Discussion

Surface structure of Mo(1 at. %):$BiVO_4$(010)

Monoclinic scheelite $BiVO_4$, (ms-$BiVO_4$) is composed of $V^{(V)}O_4$ tetrahedra and $Bi^{(III)}O_8$ dodecahedra, as shown in **Figure 1a**. Each $Bi^{(III)}O_8$ dodecahedron unit edge shares with a neighboring unit. The $V^{(V)}O_4$ tetrahedra are not in contact with each other but corner share with the $Bi^{(III)}O_8$ dodecahedra. Literature values for the standard unit cell parameters (C/2c space group setting[30, 44]) are a = 7.247 Å, b = 11.697 Å, c = 5.090 Å, and β = 134.226°, which were determined experimentally on single crystals via neutron and X-ray diffraction[45] and theoretically using density functional theory (DFT) calculations.[30] The crystallographic directions and surface indexes used in **Figure 1a**, and throughout the text, are defined within the conventional C/2c space group setting,[46] according to Zhao et al. [30]

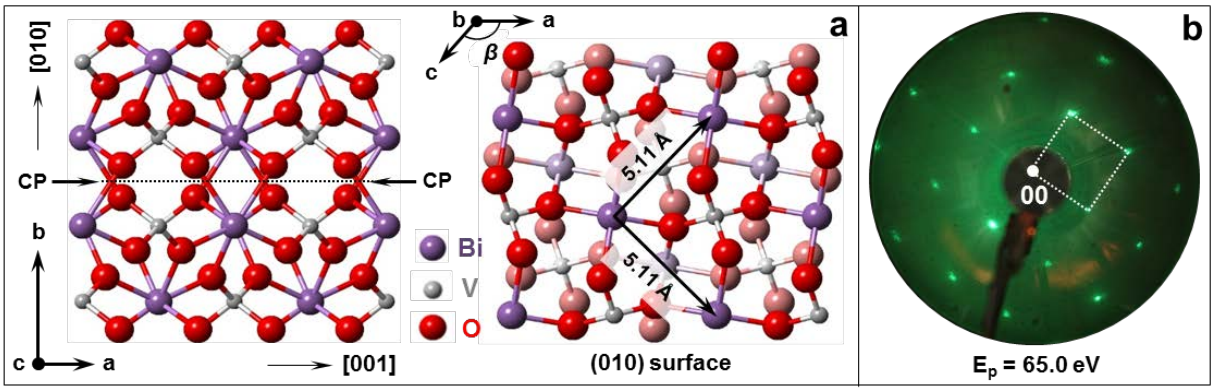

Figure 1. Structure of monoclinic scheelite $BiVO_4$ crystal and (010) surface. Figure **a** shows the crystal structure composed of VO_4 and BiO_8 coordination units, together with the predicted cleavage plane (CP) orthogonal to the [010] crystallographic direction (within the conventional C/2c space group setting).[46] Figure **b** shows the low energy electron diffraction (LEED) pattern displaying the 1×1 square pattern and the corresponding distances on the (010) surface.

Previous theoretical calculations suggest that the preferential cleavage plane for ms-$BiVO_4$ is orthogonal to the [010] crystallographic direction (*b* axis) (see **Figure 1a)** and located at ½ *b*.[44, 46] Cleavage along this plane involves the rupture of Bi–O bonds (4 Bi−O bonds per unit cell) and

leads to a surface composed of fully 4-fold coordinated V atoms, 6-fold coordinated Bi atoms and 2-fold coordinated O atoms. The preferential breaking of Bi–O bonds is a result of the Bi–O bonds in the BiO_8 dodecahedra being much weaker than the V–O bonds in the rigid VO_4 tetrahedra.[46] The resulting (010) surface has the lowest surface energy (γ) among the $BiVO_4$ crystal facets.[32, 46, 47] Moreover, the $BiVO_4$(010) surface possesses high charge carrier mobility and photocatalytic activity for water oxidation.[32, 48]

The $BiVO_4$(010) surface has a square unit cell with sides 5.11 Å in length, as recently reported by Zhao et al. (**Figure 1a**).[47] We have characterized the $BiVO_4$(010) surface using low energy electron diffraction (LEED) after the cleaning procedure described in the experimental section. Our results show that the clean crystal surface exhibits a 1×1 square LEED pattern, consistent with the (010) orientation of the surface (**Figure 1b**). To determine the surface lattice constant, we have used a LEED pattern from the $BiVO_4$ surface obtained at 100 eV primary electron kinetic energy (E_p) and calibrated it using the LEED pattern from the 1×1 unreconstructed hexagonal lattice of a Pt(111) single crystal also taken with E_p = 100 eV primary kinetic energy (see **Figure S3** and related discussion). We determined a surface lattice constant, of 5.56 ± 0.42 Å. This suggests that the cleaved (010) surface is not significantly reconstructed within the surface plane.[47]

Chemical composition determined using synchrotron-based XPS

Quantitative X-ray photoelectron spectroscopy (XPS) was used to analyze the relative concentrations and oxidation states of Bi, V, O, and Mo at the pristine Mo(1 at.%):$BiVO_4$(010) surface. The measurements were performed at room temperature and in ultra-high vacuum (UHV), with pressures of ~10^{-9} Torr. The core level spectra shown in **Figure 2** were acquired with different nominal photon energies, to provide the same photoelectron kinetic energy (200 eV) and the same information depth for each core level. At a photoelectron KE of 200 eV, the inelastic mean free path (λ_e) in $BiVO_4$ is equal to 8.3 Å (see the experimental section for further details).[37] The information depth d can be defined as the depth from which 95% of the emitted electrons are inelastically scattered (i.e. $3\lambda_e$). At KE ~ 200 eV, and taking into account our take-off angle θ of 47°, $d = 3\lambda_e \cdot \cos\theta$ = 17.0 Å and is ~ 1.5 b. We therefore probe approximately the 6 topmost layers of Mo(1 at.%):$BiVO_4$(010) with our measurements. Using the normalized area of the core level spectra shown in **Figure 2** (see Experimental section) we determined the following relative surface stoichiometry: $Mo_{0.02}$:$Bi_{1.09}V_{1.00}O_{4.04}$. The nominal relative stoichiometry for a 1

at.% Mo doped $BiVO_4$ is $Mo_{0.06}$:$Bi_{1.00}V_{1.00}O_{4.00}$. (Note that we define atomic percent as $(at.\%)_i = N_i/\sum_i N_i$.) Given that the concentration of Mo is near the detection limit of our measurements, we estimate that our measured stoichiometry is consistent with that expected for 1 at.% Mo in $BiVO_4$, or with the possibility that the Mo dopant concentration is slightly lower at the $BiVO_4$(010) surface compared to the bulk. Our results do not indicate any surface enhancement of the Mo dopant.[34]

The binding energies (BE) of the Bi $4f_{7/2}$ (159.3 eV, **Figure 2a**) and O 1s core levels (530.0 eV, **Figure 2b**) are consistent with the Bi^{3+} and O^{2-} binding energies previously observed in stoichiometric $BiVO_4$ films, single crystals and vanadate-based semiconducting oxides.[49, 50, 51] In **Figure 2c** the V 2p spectrum is shown. The $2p_{3/2}$ peak is centered at a BE of 516.9 eV. This value is in line with the V^{5+} oxidation state, as expected for the stoichiometric material.[49, 50, 51] The inset in **Figure 2c** shows the V $L_3M_{2,3}M_{4,5}$ Auger transition. It is centered at a kinetic energy of 466.4 eV. The corresponding Auger parameter (AP), defined as $AP = BE_{V\ 2p3/2} + KE_{V\ LMM}$, is equal to 983.3 eV. Since the AP value is mainly determined by the electronic polarizability of the oxygen ligands around the central metal ion,[52] the AP can be used as a measure of both the oxidation state of V and the symmetry around the central vanadium ion. For example, the AP is equal to ~984.0 eV and ~983.5 eV for vanadium in V_2O_5 (octahedral) and in $CeVO_4$ (tetrahedral), respectively.[52] In both cases vanadium is in the +5 oxidation state but the symmetry around the central V ion differs. Our AP value of 983.3 eV is close to the value for the tetrahedral VO_4^{3-} moiety in $CeVO_4$, and is consistent with the expected tetrahedral geometry of the VO_4^{3-} coordination shell in $BiVO_4$. **Figure 2d** shows the Mo 3d spectrum. The BE of the Mo $3d_{5/2}$ peak is 232.4 eV. The BE of the Mo $3d_{5/2}$ peak can be used to determine the oxidation state of the Mo dopant in $BiVO_4$. Roxlo et al.[53] and Choi et al.[54] reported a Mo $3d_{5/2}$ BE for Mo^{3+} of 228.2 eV and 228.7 eV, respectively. In contrast to this, the Mo $3d_{5/2}$ BE for Mo^{6+} ($4d^0$ configuration) is usually observed within a range of 232.2 – 232.6 eV.[54, 55] Our measured Mo $3d_{5/2}$ BE is therefore consistent with the Mo dopant being in the +6 oxidation state.

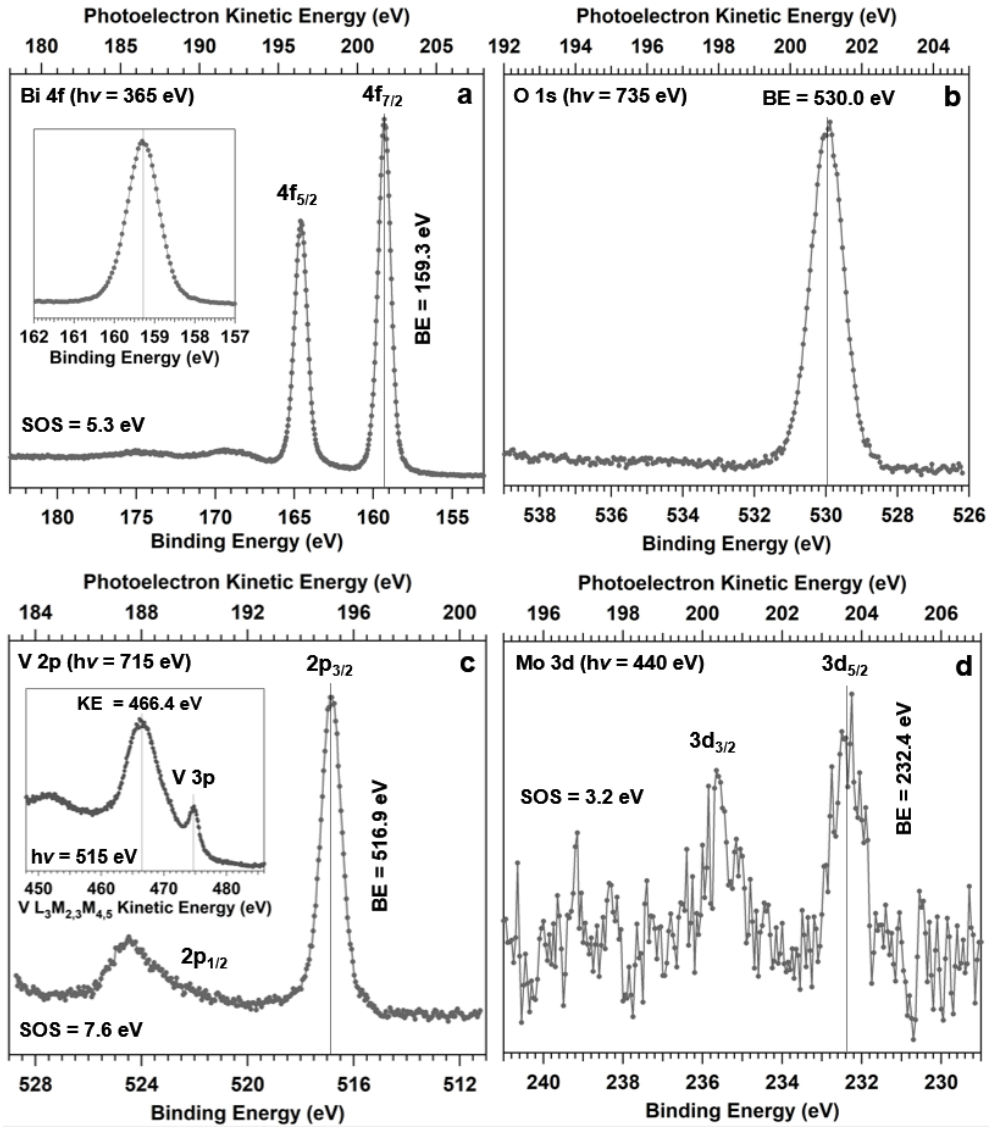

Figure 2. X-ray photoelectron spectroscopy (XPS) spectra of Mo(1 at.%):$BiVO_4$(010). **a**: Bi 4f (hν = 365 eV); **b**: O 1s (hν = 735 eV); **c**: V 2p (hν = 715 eV); **d**: Mo 3d (hν = 440 eV). The insets in Figure **a** and **c** show a magnification of the Bi $4f_{7/2}$ core level and the V Auger $L_3M_{2,3}M_{4,5}$ transition (taken at a photon energy of 515 eV), respectively.

Local geometry determined using Near Edge X-ray Absorption

To gain further information about the local bonding in the Mo-doped $BiVO_4$ single crystals, we performed near edge X-ray absorption fine structure (NEXAFS) measurements using total electron yield (TEY) detection at the V $L_{3,2}$, O K and Mo M_3 edges (**Figure 3**). These involve the following electronic transitions: V $2p_{3/2,1/2} \rightarrow$ V 3d, O 1s $\rightarrow$ O 2p, and Mo $3p_{3/2} \rightarrow$ Mo 4d, for the V $L_{3,2}$, O K and Mo M_3 edges, respectively. Using the median photon energy of each scan (530 eV for the V $L_{3,2}$ – O K edges and 398 eV for the Mo M_3 edge) as the average electron kinetic energy, we estimate inelastic mean free paths (λ_e) of 13.3 Å and 10.9 Å for the V $L_{3,2}$ – O K and

Mo M_3 edge spectra, respectively.[37] Since the take-off angle was 20° from the surface normal, the information depth ($3\lambda_e \cdot \cos\theta$) is approximately 37.4 Å (~ 3.2 *b*) and 28.9 Å (~ 2.5 *b*) for the V $L_{3,2}$ – O K and Mo M_3 edge spectra, respectively. This implies that the TEY-NEXAFS measurements are slightly less surface sensitive than the corresponding XPS data reported above. The V $L_{3,2}$ – O K edges for Mo(1 at. %):$BiVO_4$(010) and for V_2O_5 powder are shown in **Figure 3a**. In both samples, vanadium is present as V^{5+} but the coordination geometry with the oxygen ligands is different: it is tetrahedral for Mo(1 at.%):$BiVO_4$(010) and octahedral for V_2O_5. This is reflected in the different shapes of the V L edges for the two samples which is due to the inversion of the *d* orbital splitting when passing from a tetrahedral to octahedral crystal field (*e*-t_2 vs. t_{2g}-e_g, respectively). The spectral broadening of the L_2 edge is larger than the L_3 edge due to Coster-Kronig effects, rendering the L_3 edge more informative for discussing crystal field splitting values.[56]

The crystal field splitting (CFS) determined for V_2O_5 (Δ_O) is 2.9 eV, whereas for Mo(1 at. %):$BiVO_4$(010) (Δ_T) it is 2.2 eV (see **Figure 3a**). In the ionic approximation, the relationship between the Δ_O and Δ_T CFS values for a metal cation of a given oxidation state in an O^{2-} ligand field is $\Delta_T \approx 4/9\ \Delta_O$.[57] Considering the CFS value determined for V_2O_5, a CFS of about 1.3 eV would be expected for Mo(1 at.%):$BiVO_4$(010) if V ions experienced a pure undistorted tetrahedral field. The difference between the expected and measured values implies significant structural distortion which increases the energy splitting between the *e* and t_2 levels and partially removes their degeneracy. This will be further discussed in the next section.

Due to hybridization between metal states and O 2p states the O K-edge NEXAFS spectrum can provide insight into unoccupied metal states.[58] The features centered at 529.1 eV (σ*) and 530.6 eV (π*) are from hybridization between the O 2p and V 3d states.[59] The prominent peak at 534.1 eV is related to O 2p and Bi 6p hybridized states.[20] Finally, a broad feature centered at 537.5 eV indicates mixing of metal 4 sp and O 2p electrons, and O-related Rydberg states appear at higher photon energy.[59]

Figure 3b shows the Mo M_3 edge NEXAFS spectrum. The position of the M_3 edge (~ 396.5 eV) and splitting into the e (395.6 eV) and t_2 (397.1) states confirm that Mo is present as Mo^{6+} in a tetrahedral crystal field, as previously reported for Mo-doped $BiVO_4$[35] and similar to that observed for Na_2MoO_4.[60] We compared our measured values to those obtained using the multiplet approach in the CTM4XAS program.[61] Calculations were performed at a temperature of 295 K and using Slater integrals reduced to 30% of their calculated atomic values, similar to

George et al. for the $(MoO_4)^{2-}$ coordination unit.[60] The resulting final states (with no charge transfer) were convoluted with pseudo-Voigt functions, with 0.5 eV Lorentzian[62] and a 0.3 eV Gaussian broadening to account for the $3p_{3/2}$ core-hole lifetime and experimental energy resolution, respectively. The spin orbit (SO) coupling reduction parameters for the core and valence electrons were adjusted to 1.32% and 0.62%, respectively to energetically align the simulated spectra and the experimental data. The crystal field parameter (10 Dq) was set to the experimentally determined value of 1.5 eV. The simulation of the Mo^{6+} in an undistorted tetrahedron (point group T_d, **Figure 3b**) yields good agreement with the experimental data. Note that the satellite feature centered at 399.3 eV, has been attributed to ligand-to-metal charge transfer[60] and is not included in the simulation. We also compared our experimental data to a set of spectral calculations that used the same parameters as above, but instead inserted Mo^{3+} in an octahedral crystal field (point group O_h) as would be expected if the Mo dopant substituted for Bi.[63] For the sake of completeness, the 10 Dq parameter was varied from 1.5 eV to 3.0 eV. **Figure 3b** shows the resulting calculated spectra with 10 Dq steps of 0.5 eV. Neither the lineshape nor the spectral positions of the experimental data are captured by the simulations with the Mo in an octahedral field.

Combining the Mo M_3 edge NEXAFS and Mo 3d XPS results indicates that the Mo dopant is predominantly located in V tetrahedral sites at the surface with a $(MoO_4)^{-2}$ coordination shell and an oxidation state of +6. This is in apparent contrast with the DFT predictions reported by Ding et al., which show that Mo-doping introduces Mo^{3+} cations in Bi^{3+} sites in the outermost layer, whereas Mo^{6+} substitutes V^{5+} sites in the bulk.[33] On the other hand, similar results have recently been reported by Jovic et al.[22, 35] As we will discuss in the next section, the local coordination of Mo has a significant influence on the electronic properties of the Mo(1 at.%):$BiVO_4$(010) surface.

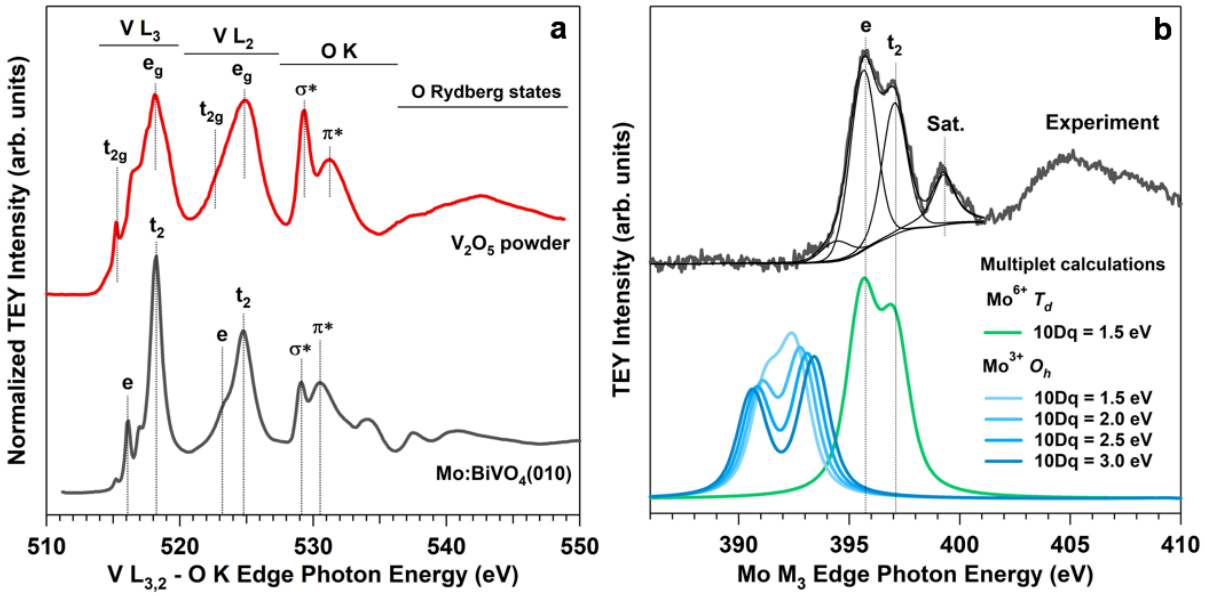

Figure 3. TEY-NEXAFS spectra; **a**: V $L_{3,2}$ – O K edges (V $2p_{3/2,1/2}$ → V 3d, O 1s → O 2p) for Mo(1 at.%):$BiVO_4$(010) (bottom) and V_2O_5 powder as a reference for V^{5+} in an octahedral crystal field (top); **b**: Experimental Mo M_3 edge (Mo $3p_{3/2}$ → Mo 4d) spectrum for Mo(1 at.%):$BiVO_4$(010) (top) and calculated Mo M_3 edges (bottom) for different oxidation states (+3, +6) and crystal field geometry (T_d, O_h), in order to simulate Mo substitution for V or Bi in the $BiVO_4$(010) surface. Note that no contributions from ligand to metal charge transfer were included in the simulations.

Electronic structure of the Mo(1 at.%):$BiVO_4$(010) surface

Previous DFT calculations predict that the V^{4+} generated by the Mo^{6+} dopant should produce a state above the valence band maximum (VBM).[32] As shown by Zhao et al.[30] and Liu et al.,[32] O 2p levels dominate the VB density of states near the VBM. This makes identifying the different elemental and orbital contributions to the VB difficult. Resonant photoelectron spectroscopy (ResPES), however, can be used to de-convolute the VB into its various elemental and orbital contributions.[64, 65, 66, 67] We have used V L_3 ResPES to understand in more detail the V contributions to the valence electronic structure. **Figure 4a** shows a ResPES VB map of Mo(1 at.%):$BiVO_4$(010) generated by acquiring VB spectra while scanning the photon energy across the V L_3 edge (**Figure 4b**). Two selected VB spectra are shown in **Figure 4c** which were taken in off- (photon energy = 514.0 eV) and on-resonance conditions (photon energy = 517.4 eV). **Figure 4d** shows a magnification of the VB spectrum around the VBM for off- and on-resonance conditions. The VBM is equal to 2.3 eV as determined from the off-resonance spectrum using the intercept method of Kraut et al.[68] Following the procedure developed by Okabayashi et al.,[69] we subtracted the off-resonance spectrum from the on-resonance one, thereby obtaining the V 3d contribution to the VB. Our findings are in agreement with the V 3d

pDOS obtained from DFT calculations which show that the middle of the VB is mainly composed of V 3d and O 2p hybridized orbitals.[20, 30, 32]

To gain further insight into the electronic structure of the (010) surface, the VB spectra were fitted with pseudo-Voigt functions as done by Cooper et al.[20] The components were then assigned to the specific molecular orbitals (MO) based on the work of Zhao et al. (see **Figure 5)**.[30] First we consider the off resonant VB spectrum in **Figure 4c**. The composition of the top of the VB in $BiVO_4$ has been explained in detail by Payne and coworkers[70] by the revised lone pair (RLP) model. The RLP model also helps to explain the origin of structural distortions in $BiVO_4$. In this model significant mixing between the Bi 6s lone pair states and O 2p states gives rise to an occupied antibonding state at the top of the VB (O $2p_\pi$ Bi 6s:, BE = 2.3 eV). This antibonding state has minority 6s character (majority Bi 6s contribution is located at the bottom of the VB). The lone pair of electrons and Bi 6s and O 2p mixing causes structural distortion of both the BiO_8 dodecahedra and the VO_4 tetrahedra. This structural distortion helps to reduce antibonding destabilization. Below the VBM weak hybridization between the vanadium e and t_2 branches and the O p_π and O p_σ orbitals gives rise to the formation of the π state centered at a BE = 4.1 eV (V-O π) which energetically overlaps with the Bi σ contribution. Strong hybridization between the vanadium e and t_2 branches with the O p_σ states leads to the formation of the σ band, observable as the intense feature in the middle of the VB at a BE = 5.8 eV (V-O σ) in **Figure 4a**.[42, 64] The Bi π state (Bi 6p self-hybridized orbitals weakly mixed with O 2p states) combined with the Bi σ (Bi 6s weakly mixed with O 2p states) and the V-O σ states contribute to the lower edge of the VB (**Figure 4c**, BE = 7.6 eV). Lastly, Bi 6s and O 2s orbitals form a weakly hybridized state, Bi-O σ,[30] which energetically overlaps with a weakly hybridized V e and O 2s state (V-O σ) at a BE = 12.2 eV (**Figure 4c**).[30]

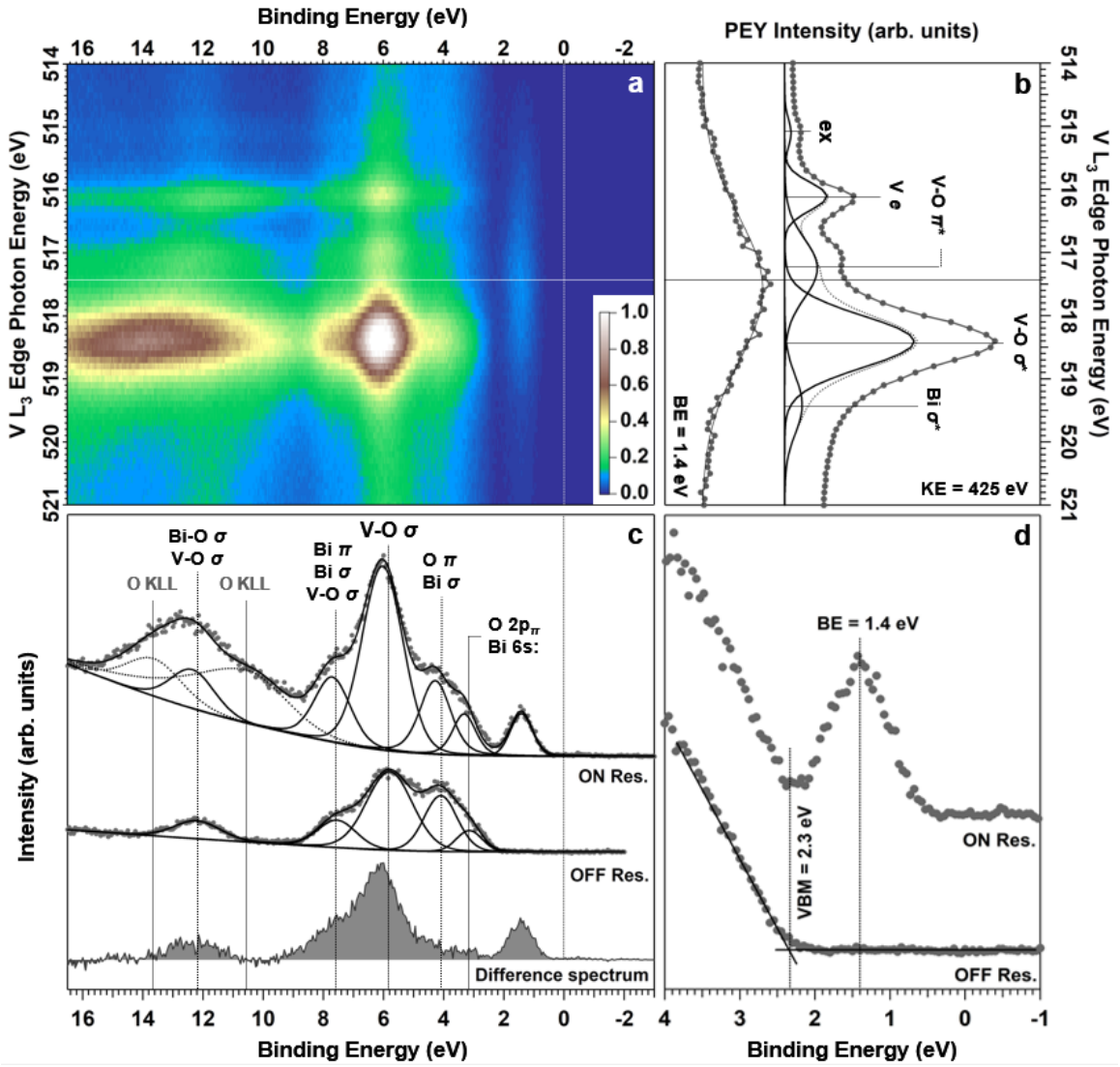

Figure 4. ResPES valence band map of Mo(1 at.%):$BiVO_4$(010) as the photon energy was scanned over the V L_3 edge, Figure **a**. Figure **b** shows the V L_3 PEY-NEXAFS spectrum together with the profile of the resonance observed above the valence band maximum (VBM). Figure **c** shows two selected VB spectra taken under off- and on-resonance conditions (photon energy equal to 514.0 eV and 517.4 eV, respectively). The O KLL Auger transitions shown as dotted lines are due to the direct O Auger emission, as the photon energy approaches the O KLL KE. The difference spectrum was obtained by subtracting the O KLL Auger contributions and the non-resonant VB spectrum from the on-resonance one. Figure **d** shows a magnification of the VBM for off- and on-resonance conditions.

Before discussing the enhancement of the VB features under resonant conditions, we first discuss the V L_3 edge PEY−NEXAFS spectrum (**Figure 4b**) in terms of the $BiVO_4$ MO diagram shown in **Figure 5**. In the NEXAFS spectrum three major peaks labelled as V e, V-O π*, and V-O σ* are observed. In addition, there is a peak, labeled ex, at low photon energies and a peak at high photon energies, labeled Bi σ*. The conduction band minimum (CBm), was identified using the first derivative of the NEXAFS spectrum and is at a photon energy of 515.9 eV (note that

DFT calculations have shown that the CBm is mainly composed of V 3d states, therefore the V L_3 edge NEXAFS spectrum should provide an accurate position of the CBm[30, 31, 32, 33]). To aid discussion, a fit of the NEXAFS spectrum is included in **Figure 4b**. The lowest photon energy state, ex, at a photon energy of approximately 515.1 eV and 0.8 eV below the CBm, is likely associated with a core hole exciton. Such a state is generated by the Coulombic interaction of the electron photoexcited from the V $2p_{3/2}$ core level and the core hole left by that electron.[71] Another possibility is excitation of an electron into a localized, small polaronic state at V^{4+} sites generated by doping with Mo.[32] DFT calculations locate this state at 0.3 eV below the CBm.[32] Significant energy shifts from the calculated value for this state might be expected due to stabilization of this state by the core hole generated during the absorption process. The next highest energy state, the *e* state, is centered at a photon energy of 516.1 eV, or about 0.2 eV above the CBm. This state corresponds to the crystal field split V $3d_{z^2}$ and $3d_{x^2-y^2}$ orbitals that are mostly unhybridized.[30] The next highest energy feature is located at a photon energy of about 517.0 eV and is about 1.1 eV above the CBm. This state is a π anti-bonding state (π^*) formed by hybridization of the V e states and O $2p_\pi$ states.[30] In this spectral region contributions from the V d_{zx} state may also be expected due to mixing with the V d_{z^2} orbital caused by distortion of the VO_4 tetrahedra in the ms-$BiVO_4$ structure.[20] The σ^* spectral feature is the most dominant peak in the spectrum and is centered at approximately 518.4 eV, or 2.5 eV above the CBm. It is generated by the higher energy CFS branch, t_2, composed of the V $3d_{xy}$, $3d_{yz}$, and $3d_{zx}$ orbitals, mixing with O $2p_\sigma$ states.[30] The Bi antibonding 6p σ^* state is located at about 3.5 eV above the CBm, and a photon energy of 519.4 eV. The Bi 6p σ^* antibonding contribution to the upper CB, although probed via the V L_3 edge resonance, is due to mixing of anisotropic Bi 6p states with O 2p states. The anisotropy is caused by significant distortion of the BiO_8 dodecahedra units. Mixing of V t_2 states with O p_σ orbitals, (**Figure 5**) leads to these state being visible in the V L_3 edge spectrum.[20, 21, 30]

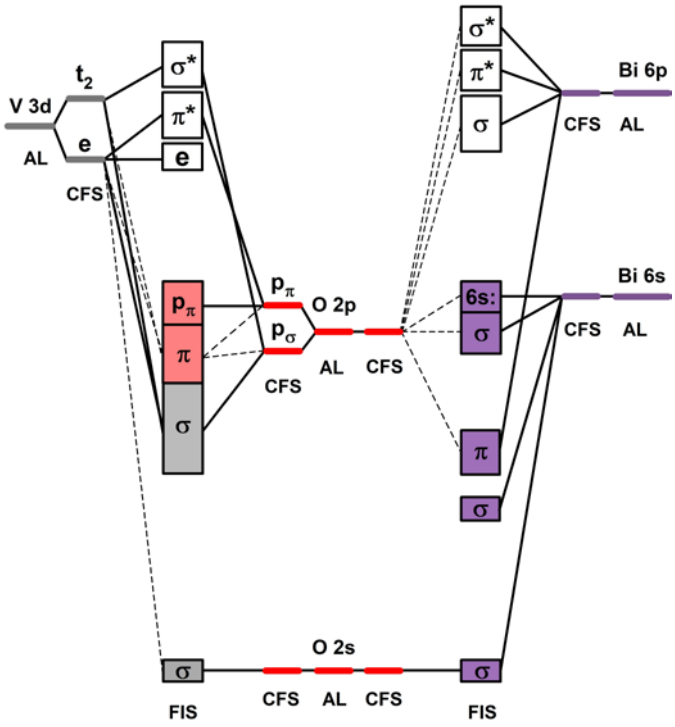

Figure 5. Molecular orbital (MO) diagram for monoclinic scheelite $BiVO_4$.[30] The solid and dashed lines represent large and small contributions of the crystal field split orbitals to the final interaction states, respectively. AL: atomic level; CFS: crystal field splitting; FIS: final interaction state.

The most evident features in the ResPES valence band map are the enhancement of the V-O σ states at BEs of 5.8 eV, 7.6 eV and 12.2 eV (**Figure 4a**). Enhancement of these states occurs at photon energies associated with the peaks of the major transitions in the V L_3 edge spectrum, hν = 516.1 eV, 517.0 eV and 518.4 eV. As expected the enhancement of the V-O σ valence states is most pronounced when in resonance with the V-O σ* state at 518.4 eV. The valence and conduction band states associated with these features have all been attributed to the molecular orbitals formed in pristine, undoped $BiVO_4$ (see above and Ref. 30). Interestingly, the ResPES map shows a feature above the valence band maximum at a BE of 1.4 eV (0.9 eV above the VBM, **Figure 4d**). The maximum intensity of this feature occurs at a photon energy of 517.4 eV (**Figure 4b**) and is not associated with any of the major peaks in the V L_3 NEXAFS spectrum. A similar spectral feature was observed by Smith et al. when performing ResPES along the shallow 3p → 3d transition on both Ti_2O_3 and V_2O_3 and attributed to resonance occurring with highly localized metal d-states.[72, 64] Jovic et al. recently observed a similar feature above VBM in a ResPES study of W and Mo doped single crystalline $BiVO_4$.[22, 35] These authors attributed this feature to highly localized V^{4+} states of *e* symmetry as a result of Mo or W doping and stated that

it is consistent with DFT calculations showing small polaron localization in V $3dz^2$ states.[32] Therefore, we also attribute the above VBM feature in the ResPES map of **Figure 4a** to a highly localized V^{4+} state induced by Mo doping, likely associated with small polaron formation.

In the study of Jovic et al., VB spectra were acquired at photon energies in resonance with specific features in the V $L_{2,3}$ edge. The highest intensity of the above VBM feature was observed when the photon energy was tuned in proximity of the V 3d *e* band.[22] However, the increased density of VB sampling as a function of photon energy in our study allows us to observe that the maximum intensity of the above VBM feature is at a photon energy of 517.4 eV. This energy is not in resonance with any of the major features observed in the V L_3 NEXAFS spectrum (**Figure 4b**). (Note that Jovic et al. observe above-VBM states in both W and Mo doped single crystalline $BiVO_4$ in off resonance conditions (hν = 275 eV) as well. These states may be due to a partially reduced surface leading to V^{4+} (see **Figure S4**). The V^{4+} produced via surface reduction is quite likely chemically distinct from the V^{4+} produced via Mo or W doping. The V^{4+} produced via doping remains coordinated with four oxygen atoms while that produced via surface reduction does not. This may lead to different resonance enhancement energies for the above VBM state for V^{4+} produced via doping compared to V^{4+} produced via surface reduction.) As stated above, the major features of the V L_3 NEXAFS spectrum have been attributed to CB states of pristine $BiVO_4$ with V in the +5 oxidation state. However, the addition of the electron through Mo doping, and subsequent small polaron formation, may cause changes in hybridization and lead to states that are distinct from the valence and conduction states of undoped $BiVO_4$. The energetic position of the resonance enhancement allows us to speculate what this state might be. The energetic position of the resonance enhancement is at the high energy side of the V-O π* band. DFT calculations have shown that this region contains states that are formed after the addition of an electron which becomes trapped at a V^{5+} site to form V^{4+} and a small polaron.[32] This is the region where the maximum of V $3d_{z^2}$ hybridized states occur and it is also the region where mixing of V $3d_{zx}$ and V $3d_{z^2}$ orbitals is expected.[20] V $3d_{zx}$ and V $3d_{z^2}$ orbital mixing is due to distortion of the VO_4 tetrahedra.[20] This suggests that V $3d_{z^2}$ states, possibly mixed with V $3d_{zx}$ states, are responsible for the above VBM resonance enhancement. The addition of the electron and small polaron formation through Mo doping induces further distortion of the VO_4 units. That this occurs is supported by DFT calculations that have shown V-O bond elongation upon small polaron formation.[32] This further distortion causes changes in the hybridization of the V $3d_{z^2}$ with O 2p states and/or mixing of V $3d_{zx}$ and V $3d_{z^2}$ orbitals which leads to the splitting of the

V-O π* state to form a state at 517.4 eV. Furthermore, this state must be highly localized (i.e., on the same V^{4+} atom as the V 2p core hole) and therefore likely associated with a small polaron formed upon Mo-doping.[64] Regardless of the precise nature of the CB state associated with the resonance enhancement of the above VBM feature, this work provides further experimental evidence for the formation of an intra-band gap small polaron state, through the self-localization of the excess electron provided by Mo doping.[28, 29, 32]

Connection to photoelectrochemistry: Energy levels on the normal hydrogen electrode scale

To put the valence band measurements and NEXAFS measurements on a common energy scale, i.e., the BE scale, the NEXAFS photon energy axis was converted into an energy relative to the Fermi energy of Mo(1 at.%):$BiVO_4$(010). This was done by placing the experimentally determined CBm (see above) at the CBm position provided by DFT calculations, i.e., 0.3 eV above the Fermi level[32,33]. The validity of this relies on the accuracy of the DFT calculations in predicting the CBm, which is composed mainly of V 3d states.[30-33]

Since reference electrode values are given relative to the vacuum level, to convert the BE scale to an electrochemical scale we need to know the work function (φ) of the Mo(1 at.%):$BiVO_4$(010) surface. The BE scale can then be converted to a scale where the vacuum level is at zero and bound electronic states are negative in energy according to:

$$E^{VAC} = -(BE + \varphi) \qquad (1)$$

where E^{VAC} is the energy relative to the vacuum level. φ can be determined by measuring the secondary electron cutoff (SEC). Using a photon energy of 47 eV, we find a φ value of 5.15 ± 0.05 eV for the Mo(1 at.%):$BiVO_4$(010) surface (see **Figure S5**). This is consistent with previous φ values reported for polycrystalline $BiVO_4$ films.[20, 21] Determination of the position of the vacuum level (E_{Vac}) allows us to provide an estimate of the electron affinity (EA) for the Mo(1 at.%):$BiVO_4$(010) surface, since EA = E_{Vac} − CBm. This value is estimated to be EA = 4.85 eV. The zero for the normal hydrogen electrode (NHE) is at −4.44 ± 0.02 eV relative to the vacuum level at standard conditions (T = 298.15 K, pH = 0).[73] This leads to:

$$E^{NHE} = -(E^{VAC} + 4.44\ eV),\ pH = 0 \qquad (2)$$

where E^{NHE} is the energy relative to the normal hydrogen electrode. However, to compare the experimentally-determined quantities with the H_2O/O_2 oxidation and H^+/H_2 reduction potentials, it is important to note that the latter are given for the standard state (pH = 0). On the other hand, the energetic values determined in this work correspond to energy levels of the Mo(1

at.%):$BiVO_4$(010) surface in vacuum. Chun et al. showed that energetic values determined in vacuum likely correspond to those at the isoelectric point of the material.[74] Since band bending is the result of a deviation from charge neutrality, a charge neutral surface should display no band bending.[75] However, in many cases semiconductors in vacuum exhibit band-bending due to non-zero surface charge. We performed depth profiling by acquiring the Bi 4f core level spectra at different photon energies to check for band-bending at the Mo(1 at.%):$BiVO_4$(010)/vacuum interface (see **Figure S5)**. The photoelectron kinetic energy was changed between ~200 eV and ~575 eV, corresponding to changes in the photoelectron inelastic mean free path (information depth) of 7.2 Å (21.6 Å) to 14.1 Å (42.3 Å). The absence of any significant binding energy shift or changes in peak width of the Bi 4f core level at the different kinetic energies (**Figure S5**) allows us to conclude that the clean Mo(1 at.%):$BiVO_4$(010) surface in UHV does not exhibit band bending and is therefore representative of flat-band conditions.[68] The absence of band bending also implies a homogeneous charge distribution and therefore distribution of ionized Mo dopants and reduced V. This is consistent with the surface concentration of Mo^{6+} being equal to the expected nominal bulk concentration (see above). Our measured energetic values should therefore be equivalent to those for a pH at which the surface charge is zero. This implies that a correction factor for the change in potential with pH needs to be taken into account when converting the energetic values relative to the vacuum (E^{VAC}) level to those versus NHE (E^{NHE}). For several metal oxides it has been found that the energy levels change by approximately 0.06 eV per pH unit.[76] Since the isoelectric point of $BiVO_4$ in aqueous solution has been experimentally and theoretically determined to be at pH 3.5,[77,78] this correction factor is equal to 0.21 eV, and

$$E^{NHE} = -(E^{VAC} + 4.44\ eV - 0.21\ eV) \qquad (3)$$

Table 1 and **Figure 6** report values for the VBM, CBm, small polaron band and Fermi level on the three different energy scales. The position of the VBM is 1.99 eV below the water oxidation potential, whereas the small polaron state is located at the midpoint between the two aforementioned levels. This state may act as an effective hole trap and/or recombination center and hinder charge transfer to the electrolyte thereby reducing water oxidation activity. On the other hand, the state may act as an effective intermediate state for hole transfer to the electrolyte.

Table 1. Experimentally-determined energetic positions of VBM, small polaron band, Fermi level and CBm for Mo(1 at.%):BiVO4(010) relative to the Fermi level (E_F), vacuum level (E_{VAC}), and normal hydrogen electrode (NHE) under standard conditions (T = 298.15 K, pH = 0).

	E rel. E_F (BE) (eV)	**E rel. E_{VAC} (eV)**	**E rel. NHE (eV)**ǂ ǂ Standard conditions: T = 298.15 K, pH = 0
VBM	-2.3	-7.45	3.22
Small polaron band	-1.4	-6.55	2.32
Fermi level	0.0	-5.15	0.92
CBm	+0.3	-4.85	0.62
$E^{\ominus}$ **H_2O/O_2**		-5.67	1.23
$E^{\ominus}$ **H^+/H_2**		-4.44	0.00

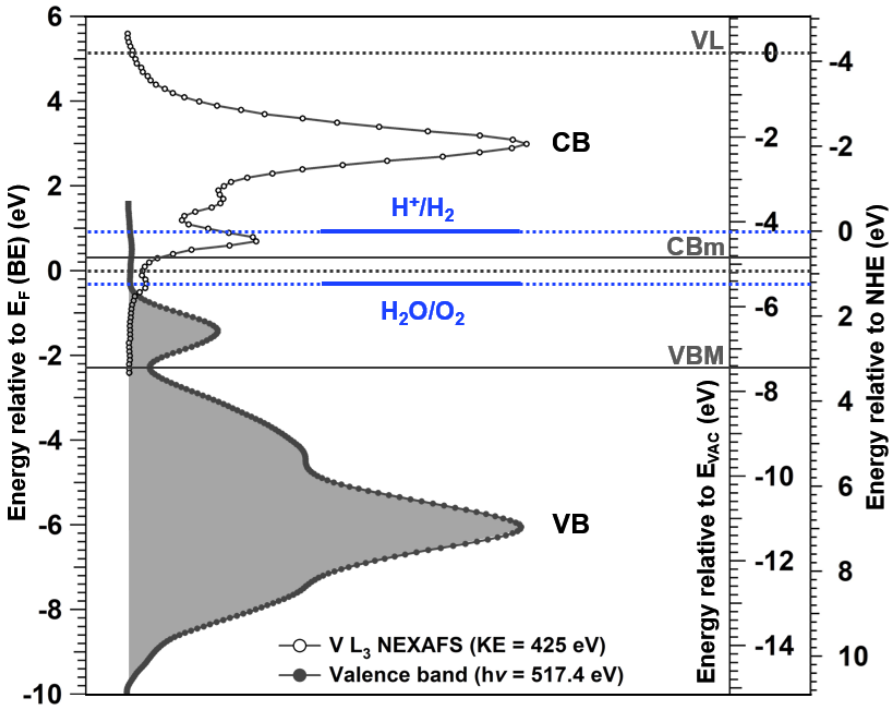

Figure 6. Valence band (VB) and conduction band (CB) states relative to the Fermi level (E_F), vacuum level (E_{VAC}), and normal hydrogen electrode (NHE) under standard conditions (T = 298.15 K, pH = 0). For comparison, the H_2O/O_2 oxidation and the H^+/H^2 reduction standard potentials are shown. The plotted CB states are from the V L_3 NEXAFS spectrum, whereas the VB states are from the VB spectrum taken in resonance with the above VBM state. For details and numerical values, see text and **Table 1**, respectively. BE: binding energy; VBM: valence band maximum; CBm: conduction band minimum; VL: vacuum level.

Conclusions

We have carried out a detailed structural, chemical and electronic investigation of the Mo(1 at.%):$BiVO_4$(010) surface. LEED indicates a surface that is not significantly laterally reconstructed from a bulk termination of the $BiVO_4$ crystal. Synchrotron-based soft X-ray spectroscopy indicates a surface chemical composition consistent with neither surface enhancement nor depletion of any of the chemical constituents. NEXAFS measurements across the Mo M_3 edge indicate that Mo occupies sites of tetrahedral coordination. This result, in combination with the measured +6 oxidation state of Mo, is consistent with V substitution by Mo at the surface. V L_3 resonant photoelectron spectroscopy (ResPES) of the valence band shows an intra-band gap state likely associated with small polaron formation. The small polaron is formed via electron donation from the Mo dopant to V^{5+} to create V^{4+} and leads to an occupied state at a binding energy of 1.4 eV, located 0.9 eV above the VBM. Additional distortion of the VO_4 tetrahedra upon electron localization induces a new state within the conduction band as indicated by resonant enhancement of the above VBM feature at 517.4 eV. This photon energy is not in resonance with any of the main features of the pristine $BiVO_4$ absorption spectrum. This new state may be the result of splitting of the V $3d_{z^2}$ orbital or V $3d_{z^2}$ – V $3d_{zx}$ orbital hybridization. Finally, we measured a work function of 5.15 eV for the (010) surface of Mo(1 at.%):$BiVO_4$. This allows us to put the electronic energy levels on an electrochemical scale. The small polaron formed by Mo doping is located midway between the VBM and the water oxidation potential. This likely has a strong influence on the photoelectrochemical performance of $BiVO_4$-based water splitting photoanodes by effecting the recombination of charge carriers and charge mobility at the surface.

ASSOCIATED CONTENT

Supporting Information

The Supporting Information (SI) is available free of charge on the ACS Publications website. SI contains the C 1s core level acquired on the clean single crystalline Mo(1 at.%):$BiVO_4$(010) surface in ultra-high vacuum, depth profiling at the Bi 4f core level of the clean single crystalline Mo(1 at.%):$BiVO_4$(010) surface in ultra-high vacuum, the determination of the surface lattice constant using low electron energy diffraction (LEED) for the clean single crystalline Mo(1 at.%):$BiVO_4$(010) surface in ultra-high vacuum, V 2p and valence band spectra for a

stoichiometric and partially reduced surface, secondary electron cut off and valence band for the work function determination of the clean single crystalline Mo(1 at.%):$BiVO_4$(010) surface in ultra-high vacuum.

AUTHOR INFORMATION

Corresponding Author

*E-mail: david.starr@helmholtz-berlin.de.

ORCID

Marco Favaro: 0000-0002-3502-8332

Silvia Nappini: 0000-0002-4944-5487

Igor Píš: 0000-0002-5222-9291

Elena Magnano: 0000-0001-6465-807

Hendrik Bluhm : 0000-0001-9381-3155

Roel van de Krol: 0000-0003-4399-399

David E. Starr: 0000-0002-6718-7557

Notes

The authors declare no competing financial interest.

ACKNOWLEDGEMENTS

The authors would like to thank Mario Brützam of the Leibniz Institut für Kristallzüchtung (IKZ) in Berlin for growing the bismuth vanadate crystals, and Michael Kanis of the Helmholtz-Zentrum Berlin for help with their preparation. We would also like to extend our thanks to Dr. Nazmul Islam of the Helmholtz-Zentrum Berlin for his advice and assistance with cutting the $BiVO_4$ crystals. This research was partially conducted at the Advanced Light Source of the Lawrence Berkeley National Laboratory, a DOE Office of Science User Facility under contract no. DE-AC02-05CH11231. This work was supported by the German Federal Ministry of Education and Research (BMBF project “JointLab - Grundlagen elektrochemischer Phasengrenzen”, GEP, #13XP5023C). M.F. gratefully acknowledges the Short Mobility Program STM 2016 (CUP 52I16000790005) and STM 2017 (CUP B53C17000270005) of the Consiglio Nazionale delle Ricerche (CNR, Italy). H.B. acknowledges support by the Director, Office of Science, Office of Basic Energy Sciences, and by the Division of Chemical Sciences,

Geosciences and Biosciences of the U.S. Department of Energy under Contract No. DE-AC02-05CH11231.

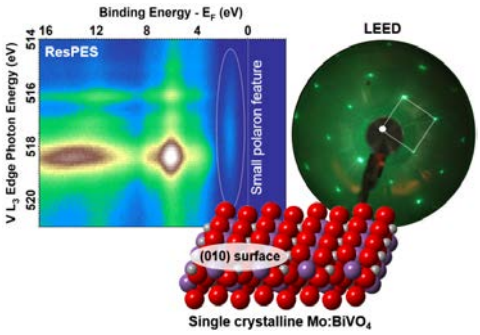
Binding Energy - E_F (eV)
16
12
8
4
0
LEED
ResPES
V L_3 Edge Photon Energy (eV)
514
516
518
520
Small polaron feature
(010) surface
Single crystalline Mo:$BiVO_4$

TOC Graphic

REFERENCES

(1) Lewis, N. S.; Nocera, D. G. Powering the planet: Chemical challenges in solar energy utilization. *Proc. Natl. Acad. Sci.* **2006,** *103*, 15729-15735.

(2) Gust, D.; Moore, T. A.; Moore, A. L. Mimicking photosynthetic solar energy transduction. *Acc. Chem. Res.* **2001,** *34*, 40-48.

(3) Chu, S.; Cui, Y.; Liu, N. The path towards sustainable energy. *Nat. Mater.* **2017,** *16*, 16-22.

(4) Sivula, K.; van dr Krol, R. Semiconducting materials for photoelectrochemical energy conversion. *Nat. Rev. Mater.* **2016,** *1*, 15010.

(5) Barton, E. E.; Rampulla, D. M.; Bocarsly, A. B. Selective solar-driven reduction of CO_2 to methanol using a catalyzed p-GaP based photoelectrochemical cell. *J. Am. Chem. Soc.* **2008,** *130*, 6342-6344.

(6) Morris, A. J.; Meyer, G. J.; Fujita, E. Molecular approaches to the photocatalytic reduction of carbon dioxide for solar fuels. *Acc. Chem. Res*., **2009,** *42*, 1983-1994.

(7) Centi, G.; Perathoner, S. Opportunities and prospects in the chemical recycling of carbon dioxide to fuels. *Catalysis Today*, **2009,** *148*, 191-205.

(8) Walter, M. G.; Warren, E. L.; McKone, J. R.; Boettcher, S. W.; Mi, Q., Santori; E. A., Lewis; N. S. Solar water splitting cells. *Chem. Rev.* **2010,** *110*, 6446-6473.

(9) Sun, J.; Zhong, D. K.; Gamelin, D. R. Composite photoanodes for photoelectrochemical solar water splitting. *Energy Environ. Sci.* **2010,** *3*, 1252-1261.

(10) Tachibana, Y.; Vayssieres, L.; Durrant, J. R. Artificial photosynthesis for solar water-splitting. *Nat. Photon.* **2012,** *6*, 511-518.

(11) Carraro, F.; Calvillo, L.; Cattelan, M.; Favaro, M.; Righetto, M.; Nappini, S.; Píš, I.; Celorrio, V.; Fermín, D. J.; Martucci, A.; Agnoli, S.; Granozzi, G. Fast one-pot synthesis of MoS_2/crumpled graphene p–n nanonjunctions for enhanced photoelectrochemical hydrogen production. *ACS Appl. Mater. Interfaces*, **2015,** *7*, 25685-25692.

(12) Ampelli, C.; Tavella, F.; Genovese, C.; Perathoner, S.; Favaro, M.; Centi, G. Analysis of the factors controlling performances of Au-modified TiO_2 nanotube array based photoanode in photo-electrocatalytic (PECa) cells. *J. Energy Chem.* **2017,** *26*, 284-294.

(13) Ager, J. W. Photoelectrochemical approach for water splitting. In *Solar to Chemical Energy Conversion*; Sugiyama, M., Fujii, K., Nakamura, S., Eds.; Springer International Publishing: Switzerland, 2016; pp 249-260.

(14) Yang, J.; Cooper, J. K.; Toma, F. M.; Walczak, K. A.; Favaro, M.; Beeman, J. W.; Hess, L. H.; Wang, C.; Zhu, C.; Gul, S.; Yano, J.; Kisielowski, C.; Schwartzberg, A.; Sharp, I.D. A multifunctional biphasic water splitting catalyst tailored for integration with high-performance semiconductor photoanodes. *Nat. Mater.* **2017,** *16*, 335-341.

(15) Abdi, F. F.; Berglund, S. P. Recent developments in complex metal oxide photoelectrodes. *J. Phys. D: Appl. Phys.* **2017,** *50*, 193002.

(16) Park, Y.; McDonald, K. J.; Choi, K.-S. Progress in bismuth vanadate photoanodes for use in solar water oxidation. *Chem. Soc. Rev.* **2013,** *42*, 2321-2337.

(17) Abdi, F. F.; Han, L.; Smets, A. H. M.; Zeman, M.; Dam, B.; van de Krol, R. Efficient solar water splitting by enhanced charge separation in a bismuth vanadate-silicon tandem photoelectrode. *Nat. Commun.* **2013,** *4*, 2195.

(18) Huang, Z.-F.; Pan, L.; Zou, J.-J.; Zhang, X.; Wang, L. Nanostructured bismuth vanadate-based materials for solar-energy-driven water oxidation: a review on recent progress. *Nanoscale* **2014,** *6*, 14044-14063.

(19) Sharp, I. D.; Cooper, J. K.; Toma, F. M.; Buonsanti, R. Bismuth vanadate as a platform for accelerating discovery and development of complex transition-metal oxide photoanodes. *ACS Energy Lett.* **2017,** *2*, 139-150.

(20) Cooper, J. K.; Gul, S.; Toma, F. M.; Chen, L.; Glans, P.-A.; Guo, J.; Ager, J. W.; Yano, J.; Sharp, I. D. Electronic structure of monoclinic $BiVO_4$. *Chem. Mater.* **2014,** *26*, 5365-5373.

(21) Cooper, J. K.; Gul, S.; Toma, F. M.; Chen, L.; Liu, Y.-S.; Guo, J.; Ager, J. W.; Yano, J.; Sharp, I. D. Indirect bandgap and optical properties of monoclinic bismuth vanadate. *J. Phys. Chem. C* **2015,** *119*, 2969-2974.

(22) Jovic, V.; Laverock, J.; Rettie, A. J. E.; Zhou, J.-S.; Mullins, C. B.; Singh, V. R.; Lamoureux, B.; Wilson, D.; Su, T.-Y.; Jovic, B.; Bluhm, H.; Söhnel T.; Smith K. E. Soft X-ray spectroscopic studies of the electronic structure of M:$BiVO_4$ (M = Mo, W) single crystals. *J. Mater. Chem. A* **2015,** *3*, 23743-23753.

(23) Pihosh, Y.; Turkevych, I.; Mawatari, K.; Uemura, J.; Kazoe, Y.; Kosar, S.; Makita, K.; Sugaya, T.; Matsui, T.; Fujita, D.; Tosa, M.; Kondo M.; Kitamori T. Photocatalytic generation of hydrogen by core-shell WO_3/$BiVO_4$ nanorods with ultimate water splitting efficiency. *Sci. Rep.* **2015,** *5*, 11141.

(24) Kim, J. H.; Jang, J. W.; Jo, Y. H.; Abdi, F. F.; Lee, Y. H.; van de Krol, R.; Lee, J. S. Hetero-type dual photoanodes for unbiased solar water splitting with extended light harvesting. *Nat. Commun.* **2016,** *7*, 13380.

(25) Landau, L. D.; Pekar, S. I. Effective mass of a polaron, *Ukr. J. Phys.* **2008,** *53*, 71-74.

(26) Abdi, F. F.; Savenije, T. J.; May, M. M.; Dam, B.; van de Krol, R. The origin of slow carrier transport in $BiVO_4$ thin film photoanodes: a time-resolved microwave conductivity study. *J. Phys. Chem. Lett.* **2013,** *4*, 2752-2757.

(27) Aiga, N.; Jia, Q.; Watanabe, K.; Kudo, A.; Sugimoto, T.; Matsumoto, Y. Electron−phonon coupling dynamics at oxygen evolution sites of visible-light-driven photocatalyst: Bismuth Vanadate. *J. Phys. Chem. C* **2013,** *117*, 9881-9886.

(28) Ziwritsch, M.; Müller, S.; Hempel, H.; Unold, T.; Abdi, F. F.; van de Krol, R.; Friedrich, D.; Eichberger, R. Direct time-resolved observation of carrier trapping and polaron conductivity in $BiVO_4$. *ACS Energy Lett.* **2016,** *1*, 888-894.

(29) Rettie, A. J. E.; Chemelewski, W. D.; Emin, D.; Mullins, C. B. Unravelling small-polaron transport in metal oxide photoelectrodes. *J. Phys. Chem. Lett.* **2016,** *7*, 471-479.

(30) Zhao, Z.; Li, Z.; Zou, Z. Electronic structure and optical properties of monoclinic clinobisvanite $BiVO_4$. *Phys. Chem. Chem. Phys.* **2011,** *13*, 4746-4753.

(31) Oshikiri, M.; Boero, M. Water molecule adsorption properties on the $BiVO_4$ (100) surface. *J. Phys. Chem. B* **2006,** *110*, 9188-9194.

(32) Liu, T.; Zhou, X.; Dupuis, M.; Li, C. The nature of photogenerated charge separation among different crystal facets of $BiVO_4$ studied by density functional theory. *Phys. Chem. Chem. Phys.* **2015,** *17*, 23503-23510.

(33) Ding, K.; Chen, B.; Fang, Z.; Zhang, Y.; Chen, Z. Why the photocatalytic activity of Mo-doped $BiVO_4$ is enhanced: a comprehensive density functional study. *Phys. Chem. Chem. Phys.* **2014,** *16*, 13465-13476.

(34) Luo, W.; Wang, J.; Zhao, X.; Zhao, Z.; Li, Z.; Zou, Z. Formation energy and photoelectrochemical properties of $BiVO_4$ after doping at Bi^{3+} or V^{5+} sites with higher valence metal ions. *Phys. Chem. Chem. Phys.* **2013,** *15*, 1006-1013.

(35) Jovic, V.; Rettie, A. J. E.; Singh, V. R.; Zhou, J.; Lamoureux, B.; Mullins, C. B.; Bluhm, H.; Laverock, J.; Smith K. E. A soft X-ray spectroscopic perspective of electron localization and transport in tungsten doped bismuth vanadate single crystals. *Phys. Chem. Chem. Phys.* **2016,** *18*, 31958-31965.

(36) Ogletree, D. F.; Bluhm, H.; Lebedev, G.; Fadley, C. S.; Hussain, Z.; Salmeron, M. A differentially pumped electrostatic lens system for photoemission studies in the millibar range. *Rev. Sci. Inst.* **2002,** *73*, 3872-3877.

(37) Smekal, W.; Werner, W. S. M.; Powell, C. J. Simulation of electron spectra for surface analysis (SESSA): a novel software tool for quantitative Auger-electron spectroscopy and X-ray photoelectron spectroscopy. *Surf. Interface Anal.* **2005**, *37*, 1059-1067.

(38) Yeh, J. J.; Lindau, I. Atomic subshell photoionization cross sections and asymmetry parameters: $1 \leqslant Z \leqslant 103$. *Atomic Data and Nuclear Data Tables*, **1985,** *32*, 1-155. To retrieve the photoionization cross section for the set photon energy, the cross sections reported in this reference were spline-interpolated within a spectral range of 5.0 eV centered on the set photon energy.

(39) Zangrando, M.; Finazzi, M.; Paolucci, G.; Comelli, G.; Diviacco, B.; Walker, R. P.; Cocco, D.; Parmigiani, F. BACH, the beamline for advanced dichroic and scattering experiments at ELETTRA. *Rev. Sci. Instr.* **2001,** *72*, 1313.

(40) S. Tougaard. Practical algorithm for background subtraction. *Surf. Sci.* **1989,** *216*, 343-360.

(41) S. Evans. Curve synthesis and optimization procedures for X-ray photoelectron spectroscopy. *Surf. Interface Anal.* **1991**, *17*, 85-93.

(42) Muñoz-Flores, J.; Herrera-Gomez, A. Resolving overlapping peaks in ARXPS data: The effect of noise and fitting method. *J. Electron Spectrosc. Relat. Phenom.* **2012,** *184*, 533-541.

(43) Tougaard, S.; Jansson, C. Comparison of Validity and Consistency of Methods for Quantitative XPS Peak Analysis. *Surf. Interface Anal.* **1993,** *20*, 1013-1046.

(44) Liu, J.-C.; Chen, J.-P.; Li, D.-Y. Crystal structure and optical observations of $BiVO_4$. *Acta Phys. Sin.* **1983,** *32*, 1053-1060.

(45) Sleight, A. W.; Chen, H. Y.; Ferretti, A.; Cox, D. E. Crystal growth and structure of $BiVO_4$. *Mater. Res. Bull.* **1979,** *14*, 1571-1581.

(46) Li, G.-L. First-principles investigation of the surface properties of fergusonite-type monoclinic $BiVO_4$ photocatalyst. *RSC Adv.* **2017,** *7*, 9130-9140.

(47) Zhao, Z.; Li, Z.; Zou, Z. Structure and energetics of low-index stoichiometric monoclinic clinobisvanite $BiVO_4$ surfaces. *RSC Adv.* **2011,** *1*, 874 - 883.

(48) Tan, H. L.; Wen, X.; Amal, R.; Nq, Y. H. $BiVO_4$ {010} and {110} relative exposure extent: governing factor of surface charge population and photocatalytic activity. *J. Phys. Chem. Lett.* **2016,** *7*, 1400-1405.

(49) Sawatzky, G. A.; Post, D. X-ray photoelectron and Auger spectroscopy study of some vanadium oxides. *Phy. Rev. B* **1979,** *20*, 1546-1555.

(50) Chen, L.; Alarcón-Lladó, E.; Hettick, M.; Sharp, I. D.; Lin, Y.; Javey, A.; Ager, J. W. Reactive sputtering of bismuth vanadate photoanodes for solar water splitting. *J. Phys. Chem. C* **2013,** *117*, 21635-21642.

(51) Starr, D. E.; Favaro, M.; Abdi, F. F.; Bluhm, H.; Crumlin, E. J.; van de Krol, R. Combined soft and hard X-ray ambient pressure photoelectron spectroscopy studies of semiconductor/electrolyte interfaces. *J. Electron Spectrosc. Relat. Phenom.* **2017,** *221*, 106-115.

(52) Castle, J. E.; Salvi, A. M.; Decker, F.; Moretti, G. Use of the absolute Auger parameter for vanadium in the study of the dielectric relaxation of cerium vanadate. *Surf. Interface Anal.* **2002,** *33*, 533-538.

(53) Roxlo, C. B.; Deckman, H. W.; Gland, J.; Cameron, S. D.; Chianelli, R. R. Edge surfaces in lithographically textured molybdenum disulfide. *Science*, **1987,** *235*, 1629-1631.

(54) Choi, J.-G.; Thompson, L. T. XPS study of as-prepared and reduced molybdenum oxides. *Appl. Surf. Sci.* **1996**, *93*, 143-149.

(55) Luo, W.; Wang, J.; Zhao, X.; Zhao, Z.; Li, Z.; Zou, Z. Formation energy and photoelectrochemical properties of $BiVO_4$ after doping at Bi^{3+} or V^{5+} sites with higher valence metal ions. *Phys. Chem. Chem. Phys.* **2013,** *15*, 1006-1013.

(56) Nyholm, R.; Mårtensson, N.; Lebugle, A.; Axelsson, U. Auger and Coster-Kronig broadening effects in the 2p and 3p photoelectron spectra from the metals ^{22}Ti-^{30}Zn. *J. Phys. F: Metal Phys.* **1981,** *11*, 1727-1733.

(57) Ballhausen, C. J. Introduction to Ligand Field Theory, McGraw-Hill Book Co., New York, 1962.

(58) Piper, L. F. J.; DeMasi, A.; Cho, S. W.; Preston, A. R. H.; Laverock, J.; Smith, K. E.; West, K. G.; Lu, J. W.; Wolf, S. A. Soft x-ray spectroscopic study of the ferromagnetic insulator $V_{0.82}Cr_{0.18}O_2$. *Phys. Rev. B* **2010,** *82*, 235103.

(59) Chen, B.; Laverock, J.; Newby, D.; McNulty, J. F.; Smith, K. E.; Glans, P. A.; Guo; J. H.; Qiao, R. M.; Yang, W. L.; Lees, M. R. Effects of rare-earth size on the electronic structure of $La_{1-x}Lu_xVO_3$. *J. Phys.: Condens. Matter* **2015,** *27*, 10.

(60) George, S. J.; Drury, O. B.; Fu, J.; Friedrich, S.; Doonan, C. J.; George, G. N.; White, J. M.; Young, C. G.; Cramer, S. P. Molybdenum X-ray absorption edges from 200 – 20,000 eV, the benefits of soft X-ray spectroscopy for chemical speciation. *J. Inorg. Biochem.* **2009,** *103*, 157-167.

(61) Stavitski, E.; de Groot, F.M.F. The CTM4XAS program for EELS and XAS spectral shape analysis of transition metal L edges. *Micron.* **2010,** *41*, 687-694.

(62) Lajaunie, L.; Boucher, F.; Dessapt, R.; Moreau, P. Quantitative use of electron energy-loss spectroscopy Mo-$M_{2,3}$ edges for the study of molybdenum oxides. *Ultramicroscopy* **2015,** *149*, 1-8.

(63) Lamotke, K. *Regular Solids and Isolated Singularities*. Friedr. Vieweg & Sohn, Braunschweig, 1986.

(64) Smith, K. E.; Henrich, V. E. Resonant photoemission in Ti_2O_3 and V_2O_3: Hybridization and localization of cation 3d orbitals. *Phys. Rev. B* **1988,** *38*, 9571-9580.

(65) Tchaplyguine, T.; Feifel, R.; Marinho, R. R. T.; Gisselbrecht, M.; Sorensen, S. L.; Naves de Brito, A.; Mårtensson, N.; Svensson, S.; Björneholm, O. Selective probing of the electronic structure of free clusters using resonant core-level spectroscopy. *Chem. Phys.* **2003,** *289*, 3-13.

(66) Favaro, M.; Agnoli, S.; Di Valentin, C.; Mattevi, C.; Cattelan, M.; Artiglia, L.; Magnano, E.; Bondino, F.; Nappini, S.; Granozzi, G. TiO_2/graphene nanocomposites from the direct reduction of graphene oxide by metal evaporation. *Carbon* **2014,** *68*, 319-329.

(67) Favaro, M.; Rizzi, G. A.; Nappini, S.; Magnano, E.; Bondino, F.; Agnoli, S.; Granozzi, G. A synchrotron-based spectroscopic study of the electronic structure of N-doped HOPG and PdY/N-doped HOPG. *Surf. Sci.* **2016,** *646*, 132-139.

(68) Kraut, E. A.; Grant, R. W.; Waldrop, J. R.; Kowalczyk, S. P. Precise determination of the valence-band edge in X-ray photoemission spectra: application to measurement of semiconductor interface potentials. *Phys. Rev. Lett.* **1980,** *44*, 1620-1623.

(69) Okabayashi, J.; Kimura, A.; Mizokawa, T.; Fujimori, A.; Hayashi, T.; Tanaka, M. Mn 3d partial density of states in $Ga_{1-x}Mn_xAs$ studied by resonant photoemission spectroscopy. *Phys. Rev. B* **1999,** *59*, R2486-R2489.

(70) Payne, D. J.; Robinson, M. D. M.; Egdell, R. G.; Walsh, A.; McNulty, J.; Smith, K. E.; Piper, L. F. J. The nature of electron lone pairs in $BiVO_4$. *App. Phys. Lett.* **2011,** *98*, 212110.

(71) Grioni, M.; van Acker, J. F.; Czyžyk, M. T.; Fuggle J. C. Unoccupied electronic structure and core-hole effects in the x-ray absorption spectra of Cu_2O *Phys. Rev. B* **1992**, *45*, 3309 **–** 3318.

(72) Smith, K. E.; Henrich, V. E. Molecular orbital effects on resonant photoemission from Ti_2O_3 and V_2O_3. *Sol. State Comm.* **1988,** *68*, 29 - 32.

(73) Trasatti, S. The absolute electrode potential: an explanatory note. *Pure Appl. Chem.* **1986,** *58*, 955-966.

(74) Chun, W.-J.; Ishikawa, A.; Fujisawa, H.; Takata, T.; Kondo, J. N.; Hara, M.; Kawai, M.; Matsumoto, Y.; Domen, K. Conduction and valence band positions of Ta_2O_5, TaON, and Ta_3N_5 by UPS and electrochemical methods. *J. Phys. Chem. B* **2003,** *107*, 1798-1803.

(75) Memming, R. *Semiconductor Electrochemistry, 2nd ed.*; Wiley-VCH: Weinheim, 2015.

(76) Matsumoto, Y.; Yoshikawa, T.; Sato, E. Dependence of the band bending of the oxide semiconductors on pH. *J. Electrochem. Soc.* **1989,** *136*, 1389-1391.

(77) Obregón, S.; Colón, G. On the different photocatalytic performance of $BiVO_4$ catalyst for methylene blue and Rhodamine B degradation. *J. Mol. Catal. A: Chem.* **2013,** *376*, 40-47.

(78) Ambrosio, F.; Wiktor, J.; Pasquarello, A. pH-dependet surface chemistry from first principles: application to the $BiVO_4$(010)-water interface. *ACS Appl. Mater. Interfaces* **2018,** *10*, 10011-10021.